



**HAL**  
open science

## Physical characterization of double asteroid (3905) Doppler

P. Descamps, F. Vachier, J. Berthier, J. Normand, P. Wiggins, H. de Groot, J. Coudert, V. Chojnacki, O. Labrevoir, S. Joly, et al.

► **To cite this version:**

P. Descamps, F. Vachier, J. Berthier, J. Normand, P. Wiggins, et al.. Physical characterization of double asteroid (3905) Doppler. *Icarus*, 2020, 345, pp.113726 -. 10.1016/j.icarus.2020.113726 . hal-03490332

**HAL Id: hal-03490332**

**<https://hal.science/hal-03490332>**

Submitted on 20 May 2022

**HAL** is a multi-disciplinary open access archive for the deposit and dissemination of scientific research documents, whether they are published or not. The documents may come from teaching and research institutions in France or abroad, or from public or private research centers.

L'archive ouverte pluridisciplinaire **HAL**, est destinée au dépôt et à la diffusion de documents scientifiques de niveau recherche, publiés ou non, émanant des établissements d'enseignement et de recherche français ou étrangers, des laboratoires publics ou privés.



Distributed under a Creative Commons Attribution - NonCommercial 4.0 International License

## Physical Characterization of Double Asteroid (3905) Doppler

P. Descamps<sup>1</sup>, F. Vachier<sup>1</sup>, J. Berthier<sup>1</sup>, J. Normand<sup>1</sup>, P. Wiggins<sup>2</sup>, H. de Groot<sup>3</sup>, J. Coudert<sup>4</sup>, V. Chojnacki<sup>5</sup>, O. Labrevoir<sup>6</sup>, S. Joly<sup>4</sup>, J.-P. Marcon<sup>4</sup>, S. Olimpiade<sup>4</sup>, B. Dargoui-Pister<sup>4</sup>, C. Delhaume<sup>4</sup>, T. Duval<sup>4</sup>, Y. El Farissi<sup>4</sup>, M. Giraud<sup>4</sup>, V. Grieco<sup>4</sup>, S. Kaderi<sup>4</sup>, A. Laidi<sup>4</sup>, T. Lauze<sup>4</sup>, H. Mary<sup>4</sup>, M. Medour<sup>4</sup>, F. Negre<sup>4</sup>, K. Passabet<sup>4</sup>, A. Perret<sup>4</sup>, M. Peyron<sup>4</sup>, N., Ramos<sup>4</sup>, M. Soridi<sup>4</sup>.

<sup>1</sup> Institut de Mécanique Céleste et de Calcul des Éphémérides, Observatoire de Paris, UMR8028 CNRS, 77 av. Denfert-Rochereau 75014 Paris, France

<sup>2</sup> Tooele Utah 84074, USA

<sup>3</sup> Nijmegen, Netherlands

<sup>4</sup> Lycée Victor Hugo, Carpentras, France

<sup>5</sup> Lycée Esclançon, Manosque, France

<sup>6</sup> Centre d'Astronomie, 04870 Saint-Michel l'Observatoire, France

Pages: 42

Tables: 4

Figures: 11

*Corresponding author:*

**Pascal Descamps**

IMCCE, Paris Observatory  
77, avenue Denfert-Rochereau  
75014 Paris  
France

descamps@imcce.fr

Phone: +33 (0)140512268

Fax: +33 (0)146332834

---

## Abstract

Observations of the synchronous double asteroid (3905) Doppler were carried out during a campaign of 3 months between October 2017 and December 2017. Several eclipse events of 0.2-0.3 mag were recorded. We refined the rotational period to  $50.826 \pm 0.002$ h. The J2000 ecliptic coordinates of the pole of the system are :  $\lambda = 215 \pm 2^\circ$  and  $\beta = 65 \pm 2^\circ$ .

The observed light curves have been reproduced synthetically by modeling each member of the system as an elongated ellipsoid, separated from each other by a distance equivalent to 5 times the sum of the two diameters. Assuming an identical internal composition of each component, we derived a bulk density of  $3.8 \pm 0.2$  g/cm<sup>3</sup>. Such a high density is typical of M-type asteroids.

## Keywords

Asteroids, rotation, surfaces - Satellites of asteroids - Eclipses - Photometry

---

## Introduction

Twin asteroid systems are particularly sought after because they allow not only to know their main physical characteristics, such as their mass and density, fundamental physical quantity that is otherwise difficult or impossible to obtain, but also to work on the scenarios of their formation.

Current shape knowledge of observed doubly synchronous binaries is mainly derived from photometric observation of mutual events between poorly-resolved components of the system, coupled with a theoretical approach based on hydrostatic equilibrium shapes (Leone et al., 1984). Such equilibrium shape models are elongated ellipsoids, which is a condition for a binary system to remain in a stable doubly synchronous orbit such that the mutual gravity torques exist to enforce the tidal locking. (Davis, A.B. and D.J. Scheeres, 2019). Mutual events enable measurement of the sizes and albedos of both objects, of their distinct surface compositions, and even of albedo patterns on their surfaces (Michalowski et al., 2002).

(3905) Doppler is a small main-belt asteroid. Its doubly synchronous binary nature was discovered fortuitously by graduate students in October 2013 (Hayes-Gehrke et al., 2014). The composite light curve recorded in 2013 showed amplitude greater than 1 magnitude with sudden and deep luminosity drops, correctly interpreted as conspicuous features of mutual events between two well-detached components tidally locked in doubly synchronized rotation. For observable mutual events to happen either the observer or the Sun (or both) must be temporarily aligned with a system's orbit plane. An "occultation-type" event occurs when one component of the system passes in front of, and fully or partially occults, the other component from the observer's point of view. An "eclipse-type" event takes place when the system components are aligned with the Sun and the shadow of one falls on the other.

---

Whenever the Sun and Earth have nearly equal lines of sight to the system, mutual events observable from the Earth are combinations of occultation-type and eclipse-type events.

The small system of Doppler has been hitherto never monitored through a number of aspect and phase angles, so that the position of its spin axis remains unknown. As with other binaries, the eclipses present a unique opportunity to accurately measure the bulk density as well as the full geometry of the system in terms of shapes and mutual separation.

Fig.1: To be inserted

The 2017 opposition was close to the 2013 opposition (Fig. 1) in terms of heliocentric ecliptic longitude so that it was reasonable to assume that mutual phenomena could occur again within the system. Moreover, this opposition is very *favorable* because it occurs near the perihelion putting Doppler at a distance of 1.0721au (opposition on October, 18 2017). This was the last opportunity before long (the next opposition similar to the 2013 opposition will occur in 2054, see Fig.1) of a favorable opposition able to show such mutual phenomena. In this paper, we report the results of a coordinated campaign to observe such events and better constrain the physical parameters of the system. The following opposition of 2019 was also observed although the general geometric configuration of the system could not be conducive to the observation of phenomena (Fig.1). However, it allows checking the validity of the general parameters of the system deduced from the observations of 2013 and 2017.

---

## 1. Observations

As the asteroid (3905) Doppler had an R-band magnitude of 14 at this time, all data were collected with small telescopes ( $D \leq 1\text{m}$ ) equipped with affordable CCD cameras. During three months, we performed photometric observations in the R-band. Aspect data are given in Table 1, including the date of the observation, the heliocentric longitude ( $\lambda$ ) and latitude ( $\beta$ ) of the asteroid, its phase angle ( $\alpha$ ) and its geocentric distance in au ( $r$ ).

Table 1: To be inserted
-------------------------

The preliminary determination of the rotation period gave a long period of more than 50 hours. In order to obtain a composite light curve as complete as possible, a network of observers well distributed in terrestrial longitude has been set up (see Table 2). In this way, it was possible to catch several phenomena, partially or totally. Such detections are valuable because they impose strong constraints on the global model of the system and its spatial orientation.

It was also the opportunity to set up a collaboration with two French high schools as part of a teaching project related to the photometric study of asteroids. To this end, the Haute Provence Observatory has made available a 50cm telescope equipped with a CCD 2048 x 2048 – the IRIS telescope ([iris.lam.fr](http://iris.lam.fr)) - dedicated to teachers in the framework of the program *Introduction to astronomy research for schoolchildren* driven by the Laboratoire d'astrophysique de Marseille (LAM).

---

Table 2: To be inserted
-------------------------

## 2. Period determination

The Phase Dispersion Minimization (PDM) technique (Stellingwerf, 1978) was used to search for the synodic rotation period within the photometric data. Based on a trial period, PDM bins data according to the rotational phase, where we assumed that two maxima and minima occurred per rotation, the average variance of these subsets is compared to the overall variance of the full set of observations. The best estimate of the period is that for which the ratio of the average variance within a bin to the variance of the sample, which defines the statistic  $\theta$ , reaches a minimum. This method does not assume any sinusoidal variation of the lightcurve and is well suited for unevenly spaced observations. PDM finds all periodic components or subharmonics (alias periods). Thanks to our three months long span of observations, the periodogram for light-time corrected data of (3905) Doppler shows a salient minimum ( $\theta = 0.17$ ) corresponding to the synodic fundamental period  $P_{\text{syn}} = 2.1177 \pm 0.0008\text{d}$  ( $50.826 \pm 0.002\text{ h}$ ) (Fig. 2).

Fig.2: To be inserted
-----------------------

The inferred final composite light curve is shown in Figure 3. The abscissa is the rotational phase corrected for light time. The  $m_1$  and  $m_2$  eclipsing minima occur at 0.25 and 0.75 rotational phase. The photometric accuracy is of  $\sim 0.02\text{mag}$ . Light curves exhibit two components: the fundamental rotational light curve and the eclipsing light curve. The 2017 and 2019 light curves all show a regular amplitude variation of  $\sim 0.45\text{ mags}$  identical to that recorded in 2013 when the (3905) Doppler binarity was

---

discovered. This indicates that in this dual system, the shape of each of the components is very different from a sphere, even slightly flattened. Several notches are clearly visible at the level of the minima of the light curves of 2017. These brief but significant drops come from phenomena of occultation of one of the components of the system by the other. Their shape and amplitude evolve over the duration of the three months of observation. This results from the slow change of appearance as well as the variation of the phase angle which attains  $26^\circ$  during the last observation of December 12, 2019.

Fig.3: To be inserted

### **3. A geometric model of the system**

Thanks to these notches in the nominal light curve, it will be possible to accurately determine the physical structure of the system as well as its spatial orientation. While in 2013 the magnitude drop caused by mutual occultation phenomena could reach 1.22 mag significant of a very low sub-observer latitude, during the campaign of 2017, we were able to record several phenomena of slightly variable amplitude ranging between  $\sim 0.15$  mag (October 27, 2017) and  $\sim 0.3$  mag (November 22, 2017). This means that in 2017 the system is no longer seen edge-on but its orbital plane has a slight inclination to the line of sight.

We applied a model of heterogeneous Roche equilibrium ellipsoids to the problem (Descamps, 2010) assuming the same composition for each component. In this model, the internal structure is not uniform and is described by a power law distribution. It was already successfully applied to small double asteroids such as Lúndia, Berna, Debussy and Tama (Descamps, 2010). It allows at the same time to determine the bulk density and the grain density on the surface and thus the macroscopic porosity. The

---

only parameter of this density law is the exponent  $n$ . In the case  $n = 0$ , we have a uniform mass distribution as it is the case for (90) Antiope (Descamps et al., 2009), the first double asteroid discovered (Merline et al., 2000). From such a density law, we can infer a simple relation between the bulk density  $\rho_b$  and the grain density  $\rho_g$  of the constituent material:

$$\frac{\rho_b}{\rho_g} = \frac{3}{2n+3} \quad (1)$$

Four free parameters should be fitted: the normalized angular velocity  $\Omega$ , which is a function of bulk density  $\rho_b$ , the orbital frequency  $\omega = 2\pi/P$  where  $P$  is the orbital period, the mass ratio  $q$  between the secondary and the primary, the exponent  $n$  of the internal density distribution power law and the limb-darkening parameter  $k$  if we adopt the simple Minnaert light scattering law (Minnaert, 1941). The normalized angular velocity  $\Omega$  is defined by

$$\Omega = \frac{\omega}{\sqrt{\frac{4}{3}\pi\rho_b G}} \quad (2)$$

Three of the four parameters -  $\Omega$ ,  $q$  and  $k$  - can be determined by simple graphical measurements of the light curve when the system is seen edge-on. The methodology is as follows. The duration of each event,  $\Delta T$ , when the system is observed equatorially, depends only two parameters:  $\Omega$  and  $q$ . The relationship between the relative duration  $\Delta T/P$  and the normalized angular velocity  $\Omega$  can be readily derived from the equation for spherical bodies according to appendix A :

---


$$\Omega = \sqrt{\pi^3 \frac{1+q}{(1+q^{1/3})^3} \left(\frac{\Delta T}{P}\right)^3} \quad (3)$$

In other words, whatever the ellipsoid shapes and the mass ratio  $q$ , the value of  $\Omega$  can be inferred simply by measuring the relative duration of events. To this end, we first considered the 2013 observation assuming that at this time the orbital plane lies in the line-of-sight plane. In short, the latitude of the sub-Earth point is near zero, which means that the rotation pole of the system is in the plane of the sky. The duration of each event is straightforwardly inferred from the light curve itself. We measured  $\Delta T = 2,67\text{h}$  ( $\Delta T/P = 0.052$  in orbital phase). It is then necessary to estimate the mass ratio  $q$ . This is carried out graphically from the smallest minima according to the relation (see appendix B):

$$\Delta mag_s = 2.5 \log(1+q^{2/3}) \quad (4)$$

Fig.4: To be inserted

If we adopt the reasonable assumption that the two components are identical in composition and therefore have identical albedos, it is remarkable to point out that the drop of the shallow minima depends only on the mass ratio and not on the light scattering by the surfaces. In addition, this allows us to determine very precisely the mass ratio. As for the deepest minima, it depends on both the mass ratio and the limb darkening. The magnitude drop of the first minima is of  $0.701 \pm 0.02 \text{ mag}$  (Fig. 4), we infer  $q = 0.83 \pm 0.03$  (or a size ratio of  $0.94 \pm 0.01$ ).

The knowledge of the mass ratio then makes it possible to determine the limb darkening parameter. It stems from Fig. B.2 of the annex B that the limb darkening parameter is  $k = 0.80 \pm 0.05$ , meaning a

---

strong brightness drop from disk center towards the limb and suggesting more Lambertian than lunar-like surfaces. It is mainly due to the significant phase angle at the instant of the observations (Doppler's phase angle was  $\alpha = 12^\circ$  in the observations of October 2013). Already, Parker et al. (2002) found that, different from other asteroids and the Moon, Ceres had a very high Minnaert's  $k$  of about 0.9, it was due to the fact that  $k$  is typically a strong increasing function of the phase angle ( $\alpha = 19.4^\circ$  in these observations).

By applying equation [3], we deduce the value of the normalized angular velocity  $\Omega = 0.033 \pm 0.002$  and from equation [2] we derive a formal bulk density of  $3.8 \pm 0.2 \text{ g/cm}^3$ . We must emphasize that this value results from the application of a model and not from a direct measurement. All that remains is to fit the value of the exponent  $n$  to determine the complete geometric solution, namely the triaxial ellipsoids that will model each component and their mutual separation. The main effect of the exponent is connected to the amplitude of the fundamental light curve which is of 0.45 mag. The greater the value of the exponent the greater the amplitude of the rotational light curve. Table 2 lists the best-fit values of our model. The synthetic light curve superimposed to the observation made in 2013 is shown on Fig.4. We simulated light curves by using polyhedral shape models with facets scattering the solar light according to the simple Minnaert law. We have assumed that bodies have the same scattering properties.

Fig 5 shows the deformation of the light curve as a function of the latitude of the sub-Earth point  $l_{sep}$ . Due to a high relative separation, it is remarkable to note that the phenomena cannot exist as long as is  $l_{sep}$  lower than  $8^\circ$ . This is found from the parameters of the solution because the limit angle  $l_{sep_{max}}$  is given by:

---


$$l_{sep_{maxi}} \approx \text{Arctan}\left(\frac{c_p + c_s}{d}\right) \approx \text{Arctan}\left(0.67 \frac{a_p + a_s}{d}\right) = \text{Arctan}(0.67D) = 8^\circ \quad (5)$$

The relative separation  $D$  is defined as  $(a_p + a_s)/d$ , where  $d$  is the orbital separation of the system,  $a_p$  the semi-major axis of the primary and  $a_s$  the semi-major axis of the secondary.

Fig. 6 shows the total amplitude of the light curve of Doppler and the magnitude differential between the two minima. As long as the latitude of the sub-Earth point is less than  $0.3^\circ$ , the light curve remains unchanged in amplitude, as does the differential in magnitude.

Fig.5: To be inserted

With  $n = 9$ , we derived a non-physical value of the grain density of  $28 \text{ g/cm}^3$ . It means that, despite the fact we successfully used a model in hydrostatic equilibrium inferred from the third law of Kepler, the system is clearly not in hydrostatic equilibrium. Nevertheless the inferred triaxial ellipsoids provide a good geometrical solution. Each component cannot be likened to a rotating fluid mass. We will deal with this issue in section 5.

Fig.6: To be inserted

#### 4. Pole solution

The change of shape of the light curve collected during the 2017 campaign, especially during the detected events, will enable us to determine as accurately as possible the position of the pole of the

---

system. This time we can no longer consider that the orbital plane is in the line-of-sight plane. We will therefore seek to solve the following system which gives the position of the rotation pole from simple and relevant assumptions on the latitude of the sub-Earth point  $l_{sep}$  (Descamps et al., 2007). The latitude of the sub-Earth point ( $l_{sep}$ ) and the North Pole position angle ( $n_p$ ) are related to the equatorial coordinates of the rotation pole  $(\alpha_0, \delta_0)$  and the equatorial coordinates of the asteroid  $(\alpha, \delta)$  by the following equations:

$$\begin{aligned}
\sin(l_{sep}) &= -\sin \delta_0 \sin \delta - \cos \delta_0 \cos \delta \cos(\alpha - \alpha_0) \\
\sin n_p \cos l_{sep} &= -\cos \delta_0 \sin(\alpha - \alpha_0) \\
\cos n_p \cos l_{sep} &= \sin \delta_0 \cos \delta - \cos \delta_0 \sin \delta \cos(\alpha - \alpha_0)
\end{aligned} \tag{6}$$

Fig.7: To be inserted

By taking two periods of observation for which the latitude of the sub-Earth point is known, we then obtain a system of two equations with two unknowns which it is easy to solve. We assume that  $l_{sep} = 0.0 \pm 0.3^\circ$  in 2013. This is a reasonable assumption given the amplitude of the magnitude drop (Fig.4). For the observed event of October 27, 2017 and November 22, 2017 (Table 1), Fig.6 allows us to estimate the value of  $l_{sep}$  knowing the maximum amplitude of the magnitude drop. With an amplitude of 0.6mag in October 2017 and 0.75mag in November 2017 (Fig.7), we assume  $l_{sep} \approx 5 \pm 0.5^\circ$  in October 2017 and  $l_{sep} \approx 3 \pm 0.5^\circ$  in November 2017. With these initial values, we find one unique pole solution able to account for all observations. Table 4 gives the final solutions to the system [6] for two pairs of dates. The correct solution is the one that is common to both systems. We

---

found the better solution for the pole solution in equatorial coordinates  $\alpha_0 = 240^\circ \pm 5^\circ$  and  $\delta_0 = 47^\circ \pm 5^\circ$ . In ecliptic coordinates it gives  $\lambda = 215 \pm 5^\circ$  and  $\beta = 65 \pm 5^\circ$ .

Fig.8: To be inserted

Figs. 7 and 8 show the result of the adjustment for light curves collected at different times. In 2017, the strong growth of the phase angle and the change in the appearance of the system contribute to distort the overall shape of the light curve. This is particularly noticeable during mutual events. Thus, as far as the observation of December 12, 2017 is concerned the phase angle was  $26^\circ$ , causing in particular a slight eclipse phenomenon of one component by the other, i.e., a shadow projected on the surface of the eclipsed component explains the slight plateau at the exit of phenomenon. In order to secure our pole solution, we carried out new photometric observations during the 2019 opposition with the 60cm-telescope of the Makes observatory in Reunion Island (Fig.8). The excellent agreement of the simulated light curve with the photometric observations constitutes a strong validation of the quality of the general solution presented in this work.

## 5. Discussion

Measurements of asteroid bulk density, along with data on the grain densities of analogue meteorites, provide valuable insight into asteroid porosity and internal structure. Given the bulk density that we derived ( $3.86 \pm 0.01 \text{ g/cm}^3$ ), the candidate meteoritic analogs should have a grain density no less than  $\sim 4 \text{ g/cm}^3$  which quite obviously rules out enstatite (typical density of  $3.2\text{-}3.8 \text{ g/cm}^3$ ) and carbonaceous chondrites (density of  $\sim 1.6\text{-}3.1 \text{ g/cm}^3$ ) analogues (Macke et al., 2010, Macke et al., 2011, Carry, 2012,

---

Britt et al., 2002). This density is typical of M-type asteroids (Pätzold et al., 2011, DeMeo and Carry, 2013, Shepard et al., 2017, Viikinkoski et al., 2018). So far, it has been possible to accurately measure the density of only two M-type asteroids with one or more orbiting moonlets. These are (22) Kalliope with a bulk density of  $3.4 \pm 0.2 \text{ g/cm}^3$  (Descamps et al., 2008) and (216) Kleopatra with a bulk density of  $3.6 \pm 0.4 \text{ g/cm}^3$  and a macroscopic porosity of  $\sim 30\text{-}50\%$  (Descamps et al., 2011). Furthermore, (21) Lutetia was flew by ESA Rosetta spacecraft on July 2010 and its bulk density was precisely determined to  $3.4 \pm 0.3 \text{ g/cm}^3$  (Pätzold et al., 2011). Finally, these lines of evidence tend to support the hypothesis that (3905) Doppler would be a M-type asteroid. The most likely meteoritic analogs for M-class asteroids and their associated grain densities are irons ( $\sim 7.5 \text{ g/cm}^3$ ), CH/CB/bencubbinite (metal rich) carbonaceous chondrites or silicate-bearing iron meteorites ( $\sim 5.0 \text{ g/cm}^3$ ), or even stony-iron meteorites such as mesosiderites ( $4.25 \text{ g cm}^{-3}$ ) suggested in the case of asteroid (16) Psyche (Viikinkoski et al., 2018). Vernazza et al. (2011) reported that asteroid (21) Lutetia has spectral and physical properties similar to the class of meteorites known as even enstatite chondrites ( $\sim 3.5 \text{ g/cm}^3$ ), however this analog may be ruled out due to a too low bulk density. Finally, our bulk density of  $3.86 \text{ g/cm}^3$  could suggest a macroscopic porosity ranging between 20-40%. Such high porosities are suggestive of extensively fractured or loosely packed asteroids (Britt et al., 2002, Scheeres et al., 2015).

However, the use of an inhomogeneous Roche model in the present work provided us with a physically unacceptable result in terms of macroscopic porosity or grain density (see Table 3). This means that the shapes of the components of the system are not equilibrium figures of rotating liquid masses. We can nevertheless make the hypothesis that these bodies have stopped deforming due to the combined effect of moderate porosity and high density of the material. Beyond a certain point, internal friction between boulders may have prevented any fluid-type deformation. All synchronous double systems studied so far have a much lower internal density while having equivalent macroscopic porosity. This is probably the reason why the modeling using rotating fluid masses in hydrostatic equilibrium gives good results.

---

Keeping the same bulk density but imposing a porosity of 40% (and thus a realistic grain density  $\rho_g = 7 \text{ g/cm}^3$ ), one realizes that one can find equilibrium figures which are identical to the ellipsoidal shapes found in this paper but for a lower value of the orbital period of 10.34h ( $\Omega = 0.159$ ), which implies that the system could have been much tighter in the past with a relative separation of  $D = 0.581$ , typical of small double asteroids observed so far (Descamps, 2010). Beyond this point, the system might have been able to continue to tidally evolve up to its present equilibrium state without any subsequent distortion of the shapes of both components. In other words, depending on the level of macroscopic porosity and bulk density, a loosely packed doubly synchronous asteroidal system, tidally locked, could exhibit fluid-like behavior in hydrostatic equilibrium as long as internal friction effects remain low enough to be able to counteract any deformation of the bodies. Discovery of other synchronous double systems with relative separation  $D$  significantly lower than 0.5 could provide some answers concerning the links between equilibrium figures and bulk density

---

## Appendix A: Duration of an event within a binary system

Fig.A1: To be inserted

Let  $\omega_c = \sqrt{\frac{4}{3}\pi\rho_b G}$  the surface orbit frequency for a rigid body of bulk density  $\rho_b$ , or the maximum spin rate that can be sustained by an undeformable body. At this spin rate, centrifugal forces would equal gravity at the equator of a spherical body. The normalized angular velocity  $\Omega$  is therefore defined by

$$\Omega = \frac{\omega}{\sqrt{\frac{4}{3}\pi\rho_b G}} \quad (\text{A.1})$$

Where  $G$  is the gravitational constant and  $\rho_b$  the bulk density. The synchronous system is made of two components of radius  $R_p$  (primary) and  $R_s$  (secondary) with  $R_s \leq R_p$ .  $M_p$  and  $M_s$  are the masses of the primary and the secondary respectively. Let  $q$  the secondary to primary mass ratio:  $q = (R_s/R_p)^3$ . The separation between each component of the system is equal to  $d$ . From the third law of Kepler, we have

$$\omega^2 d^3 = G(M_p + M_s) = \frac{4}{3}\pi\rho_b G R_p^3 (1+q) \quad (\text{A.2})$$

Then the specific angular momentum reads

---


$$\Omega = \sqrt{(1+q) \left( \frac{R_p}{d} \right)^3} \quad (\text{A.3})$$

Let  $\varepsilon_p = \frac{R_p}{d}$  and  $\varepsilon_s = \frac{R_s}{d}$ , the angles defined on Fig. A1. During an event of duration  $\Delta T$ , the occulting body (secondary) have described along its orbit an angle  $2\varepsilon_p + 2\varepsilon_s$ . Since the time taken to complete a complete orbit is  $P$ , the orbital period, we have

$$\frac{\Delta T}{P} = \frac{2\varepsilon_p + 2\varepsilon_s}{2\pi} = \frac{1}{\pi} (\varepsilon_p + \varepsilon_s) \quad (\text{A.4})$$

Replacing  $\varepsilon_p$  and  $\varepsilon_s$  by their expressions

$$\frac{\Delta T}{2P} = \frac{1}{\pi} \frac{R_p}{d} \left( 1 + \frac{R_s}{R_p} \right) = \frac{1}{\pi} \frac{R_p}{d} (1+q^{1/3}) \quad (\text{A.5})$$

We infer

$$\frac{R_p}{d} = \frac{1}{\pi} \frac{R_p}{d} \left( 1 + \frac{R_s}{R_p} \right) = \pi \frac{1}{(1+q^{1/3})} \frac{\Delta T}{2P} \quad (\text{A.6})$$

Hence, from equation (A.3) we derive the general relationship

$$\Omega = \sqrt{\pi^3 \frac{1+q}{(1+q^{1/3})^3} \left( \frac{\Delta T}{P} \right)^3} \quad (\text{A.7})$$

In the case of a double system have with a mass ratio very close to 1, (A.7) simplifies such that the angular velocity is then very poorly sensitive to the mass ratio

---

$$\Omega = \sqrt{\frac{\pi^3}{4} \left(\frac{\Delta T}{P}\right)^3} \quad (\text{A.8})$$

Finally, the measurement of the duration of an eclipsing event inside the system, gives the value of the specific angular frequency and therefore the value of the bulk density from equation (A.1).

---

## Appendix B: General magnitude drops in a binary system seen edge-on

Fig.B.1: To be inserted

We propose to calculate the drops in magnitude occurring within a binary system as a function of phase angle and photometric behavior of surfaces, assuming that it is seen edge-on. Furthermore, it is reasonable to assume that the two components are largely identical in composition and therefore should have very similar albedos as it was already observed for a couple of binary systems (Laver et al., 2009, Marchis et al., 2011). For example, mutual events within the binary system Patroclus-Menoetius were used to derive thermo-physical properties of the surface of both objects (Mueller et al., 2010). The observations are consistent with identical surface regolith properties. Therefore, in the rest of the work, we have assumed identical surface properties of both components. To this purpose we model the scattering by the Minnaert's function (Minnaert, 1941). The Minnaert model is an empirical photometric function with two parameters, the Minnaert albedo and the limb-darkening coefficient, representing the light scattering behavior across the surface. The bidirectional reflectance refers to the fraction of light scattered into direction  $e$  when the surface is illuminated by collimated incident light in direction  $i$ . It is the intensity of scattered radiance in a specific direction to the incident solar irradiance on a unit area of the surface. The reflectance  $r(i, e, \alpha)$  is usually a function of phase angle  $\alpha$ , incidence angle  $i$  of sunlight (through its cosine  $\mu_0 = \cos i$ ), i.e., the zenith distance of the Sun, and emission angle  $e$  (through  $\mu = \cos e$ ), i.e., the zenith distance to the observer :

$$r(i, e, \alpha) = A(\alpha) \mu_0^{k(\alpha)} \mu^{k(\alpha)-1} \quad (\text{B.1})$$

---

Where  $A(\alpha)$  and  $k(\alpha)$  are the two Minnaert parameters which are functions of  $\alpha$  and of the wavelength. It is well known that Eq. (B.1) is only a crude approximation to the scattering properties of real surfaces. However phase angle lower than  $\sim 30^\circ$ , Minnaert's law can be used as a convenient approximation (except in the immediate neighborhood of the limb where the Minnaert function predicts values approaching either infinity, when  $k$  is less than one, or zero, when  $k$  is greater than one).  $k(\alpha)$  cannot be easily interpreted according to physical properties of the surface; it presents the degree of limb darkening, e.g.  $k = 0.5$ , indicates that there is no limb darkening, while limb darkened surfaces have  $k > 0.5$ . On the condition  $k = 1$ , Minnaert model shrinks to the Lambert model which describes the reflected light behavior from high-albedo surfaces.

Let us adopt a rectangular system of coordinates, two axis of which lie in the "photometric equator". The photometric equator is the great circle passing through the subsolar and sub-earth points. Photometric longitude,  $\lambda$ , is measured along the photometric equator, and photometric latitude,  $\varphi$ , is measured along the central meridian which is the perpendicular great circle (Fig. B1). At phase angle  $\alpha$ , the photometric longitude runs from  $90^\circ$  at the limb to  $-(90^\circ - \alpha)$  at the terminator. From Fig. B1, obviously we have the following relation between  $(i, e)$  and  $(\lambda, \varphi)$  for a given phase angle :

$$\begin{aligned}\mu &= \cos e = \cos \varphi \cos \lambda \\ \mu_0 &= \cos i = \cos \varphi \cos (\lambda - \alpha)\end{aligned}\tag{B.2}$$

and the surface element

$$ds = R^2 \cos \varphi d\varphi d\lambda\tag{B.3}$$

---

Where  $R$  stands for the radius of the body. Each element of area  $ds$  on the planet is weighed by its apparent projected area ( $\cos e ds = \mu ds$ ) and surface brightness. The total light of sunlit body  $I(\alpha, R, k)$  as seen from the Earth at any particular phase will then be obtained by integrating the light element over the entire visible surface ( $\mu > 0$ )

$$I(\alpha, R, k) = \iint r(i, e, \alpha) \mu ds = R^2 \int_{-\pi/2+\alpha}^{\pi/2} \int_{-\pi/2}^{\pi/2} r(i, e, \alpha) \cos \lambda \cos^2 \varphi d\varphi d\lambda \quad (\text{B.4})$$

Let  $I_p = I(\alpha, R_p, k)$  and  $I_s = I(\alpha, R_s, k) = q^{2/3} I_p$  where  $R_p$  is the radius of the primary and  $R_s$  the radius of the secondary such that  $R_s \leq R_p$  and  $q = (R_s/R_p)^3$  the mass ratio. The shallowest magnitude drop  $\Delta mag_s$  is easily derived when the secondary is occulted by the primary (Fig. B1)

$$\Delta mag_s = 2.5 \log \left( \frac{I_p + I_s}{I_p} \right) = 2.5 \log (1 + q^{2/3}) \quad (\text{B.5})$$

It does not depend on both phase angle and scattering by surfaces. The problem is slightly more complicated in the case where the secondary occults the primary. Part of the light scattered by the primary is then intercepted by the secondary and is somehow replaced by that from the secondary. The surface area of the primary that is masked by the secondary appears hatched in Fig. B1. The intersection of the projection of the secondary on the surface of the primary defines a circular contour whose points are linked by the following relationships

$$\begin{aligned} \cos \varphi \cos \lambda &= \sqrt{1 - q^{2/3}} \\ \sin \lambda_0 &= \frac{R_s}{R_p} = q^{1/3} \end{aligned} \quad (\text{B.6})$$

The total light loss from the primary is then

$$\begin{aligned}
 I(\alpha, R_p, k, q) &= R_p^2 \int_{\text{Min}\left[-\frac{\pi}{2}+\alpha, -\lambda_0\right]}^{\lambda_0} \int_{-\varphi(\lambda)}^{\varphi(\lambda)} r(i, e, \alpha) \cos \lambda \cos^2 \varphi d\varphi d\lambda \\
 &= R_p^2 \int_{\text{Min}\left[-\frac{\pi}{2}+\alpha, -\lambda_0\right]}^{\lambda_0} \int_{-\varphi(\lambda)}^{\varphi(\lambda)} \cos^k \lambda \cos^k (\lambda - \alpha) \cos^{2k+1} \varphi d\varphi d\lambda
 \end{aligned} \tag{B.7}$$

Hence it follows that the deepest magnitude drop  $\Delta mag_d$  is expressed by

$$\Delta mag_d = 2.5 \log \left( \frac{I_p + I_s}{I_s + I_p - I(\alpha, R_p, k, q)} \right) = 2.5 \log \left( \frac{1 + q^{2/3}}{1 + q^{2/3} - I(\alpha, R_p, k, q)/I_p} \right) \tag{B.8}$$

The offset in magnitude drop is straightforward

$$dmag(\alpha, k, q) = \Delta mag_d - \Delta mag_s = 2.5 \log \left( \frac{1}{1 + q^{2/3} - I(\alpha, R_p, k, q)/I_p} \right) \tag{B.9}$$

The function  $dmag(\alpha, k, q)$  has been plotted on Fig. B.2 for different phase angles and values of the limb darkening parameter  $k$ . The offset in magnitude is an increasing function of the limb darkening parameter, however it remains below  $\sim 0.2\text{mag}$  for most of the applications.

Fig.B.2: To be inserted

---

## References

Britt, D.T., Yeomans, D., Housen, K., Consolmagno, G.J., 2002. Asteroid density, porosity and structure. In *Asteroids III*, W.F. Bottke, A. Cellino, P. Paolicchi, R. Binzel Eds (University of Arizona Press, Tucson), 103-112.

Carry, B., 2012. Density of asteroids. *Planetary and space science*, 73, 98-118.

DeMeo, F.E. and B. Carry, 2013. The taxonomic distribution of asteroids from multi-filter all-sky photometric surveys. *Icarus*, 226, 723-741.

Davis, A. and D.J. Scheeres, 2019. Doubly synchronous binary asteroid mass parameter observability. Accepted for publication in *Icarus*. arXiv preprint astro-ph/1910.04720

Descamps, P., Marchis, F., Michalowski, T., Colas, F., Berthier, J., Vachier, F., Teng-Chuen-Yu, J.-P., Peyrot, A., Payet, B., Dorseuil, J., Léonie, Y., Dijoux, T., Berrouachdi, H., Chion Hock, C. and F. Benard, 2007. Nature of the small main belt asteroid 3169 Ostro. *Icarus*, 189, 362-369.

Descamps, P., Marchis, F., Pollock, J., Berthier, J., Vachier, F., Birlan, M., Kaasalainen, M., Harris, A. W., Wong, M., Romanishin, W.J., Cooper, E.M., Kettner, K.A., Wiggins, P., Kryszczyńska, A., Polinska, M., Coliac, J.-F., Devyatkin, A., Verestchagina, I., and D. Gorshanov, 2008. New determination of the size and bulk density of the binary asteroid 22 Kalliope from observations of mutual eclipses. *Icarus*, 196, 578-600.

---

Descamps, P., Marchis, F., Michalowski, T., Berthier, J., Pollock, J., Wiggins, P., Birlan, M., Colas, F., Vachier, F., Fauvaud, S., Fauvaud, M., Sareyan, J.-P., Pilcher, F., and D.A., Klinglesmith, 2009. A giant crater on 90 Antiope ? *Icarus*, 203, 102-111.

Descamps, P., 2010. Equilibrium figures of inhomogeneous synchronous binary asteroids. *Icarus*, 207, 758-768.

Descamps, P., Marchis, F., Berthier, J., Emery, J.P., Duchêne, G., de Pater, I., Wong, M.H., Lim, L., Hammel, H.B., Vachier, F., Wiggins, P., Teng-Chuen-Yu, J.-P., Peyrot, A., Pollock, J., Assafin, M., Vieira-Martins, R., Camargo, J.I.B., Braga-Ribas, F., and B. Macomber, 2011. Triplancty and physical characteristics of asteroid (216) Kleopatra. *Icarus*, 211, 1022-1033.

Hayes-Gehrke, M.N., Maroulis, M., Bartek, A., Garcia, E., Greenebaum, R., Basile, T., Lee, S.M., Bent, B., Oliver, N., Koester, K., Franco, L., 2014. Lightcurve analysis of main-belt binary system 3905 Doppler. *Minor Planet Bulletin*, 41, 72.

Laver, C., de Pater, I., Marchis, F., Adamkovics, M., and M.H. Wong, 2009. Component-resolved near-infrared spectra of the (22) Kalliope system. *Icaus*, 204, 574-579.

Leone, G., Farinella, P., Paolicchi, and V. Zappala, 1984. Equilibrium models of binary asteroids. *Astron. Astrophys.* 140, 265-272.

Macke, R.J., Consolmagno, G.J., Britt, D.T., and Hutson, M.L., 2010. Enstatite chondrite density, magnetic susceptibility, and porosity . *Meteoritics & Planetary Science*, 45, 1513-1526.

---

Macke, R.J., Consolmagno, G.J., and Britt, D.T., 2011. Density, porosity, and magnetic susceptibility of carbonaceous chondrites. *Meteoritics & planetary science*, 46, 1842-1862.

Marchis, F., Enriquez, J.E., Emery, J.P., Berthier, J., Descamps, P. and F. Vachier, 2011. The origin of 90 Antiope from component-resolved near-infrared spectroscopy. *Icarus*, 213, 252-264.

Merline, W.J., Close, L.M., Dumas, C., et al. 2000. *BAAS*, 32, 1306.

Michalowski, T., Colas, F., Kwiatkowski, T., Kryszczyńska, A., Velichko, F.P., and S., Fauvaud, 2002. Eclipsing events in the binary system of the asteroid 90 Antiope. *Astron. Astrophys.* 396, 293-299.

Minnaert, M., 1941. The reciprocity principle in lunar photometry. *Astrophys. J.*, 93, 403-410.

Mueller, M., Marchis, F., Emery, J.P., Harris, A.W., Mottola, S., Hestroffer, D., Berthier, J., and Mario di Martino, 2010. Eclipsing binary Trojan asteroid Patroclus: Thermal inertia from Spitzer observations. *Icarus*, 205, 505-515.

Pätzold, M., Andert, T.P., Asmar, S.W., Anderson, J.D., Barriot, J.-P., Bird, M.K., Häusler, B., Hahan, M., Tellman, S., Sierks, H., Lamy, P. and Weiss, B.P, 2011. Asteroid 21 Lutetia : Low mass, High density. *Science*, 34, 491.

Parker, J. W., Stern, S. A., Thomas, P. C., Festou, M., Merline, W. J., Young, E. F., Binzel, R. P., Lebofsky, L. A., 2002. Analysis of the First Disk-resolved Images of Ceres from Ultraviolet Observations with the Hubble Space Telescope. *The Astronomical Journal*, 123, 549-557.

Scheeres, D.J., Britt, D., Carry, B., and K.A. Holsapple, 2015. Asteroid interiors and morphology. Asteroid IV, Patrick Michel, Francesca E. DeMeo, and William F. Bottke (eds.), University of Arizona Press, Tucson, 754-766.

---

Shepard, M.K., Richardson, J., Taylor, P.A., Rodriguez-Ford, L.A., Conrad, A., de Pater, I., Adamkovic, M., de Kleer, K., Males, J.R., Morzinski, K.M., Close, L.M., Kaasalainen, M., Viikinkoski, M., Timerson, B., Reddy, V., Magri, C., Nolan, M.C., Howell, E.S., Benner, L.A.M. and J.D. Giorgini, 2017. Radar observations and shape model of asteroid 16 Psyche. *Icarus*, 281, 388-403.

Stellingwerf, R.F., 1978. Period determination using phase dispersion minimization. *Astrophys. Journal*, 224, 953-960.

Viikinkoski, M., Vernazza, P., Hanuš, J., Le Coroller, H., Tazhenova, K., Carry, B., Marsset, M., Drouard, A., Marchis, F., Felick, R., Fusco, T., Ďurech, J., Birlan, M., Berthier, J., Bartczak, P., Dumas, C., Castillo-Rogez, J., Cipriani, F., Colas, F. and M. Ferrais, 2018. (16) Psyche: A mesosiderite-like asteroid? *Astronomy and Astrophysics*, 619, L3.

**Table 1:** 2003-2007 observational circumstances. The heliocentric longitude ( $\lambda$ ) and latitude ( $\beta$ ) of the asteroid, its phase angle ( $\alpha$ ) and its geocentric distance in UA ( $r$ ).

Date	$\lambda$ ( $^{\circ}$ )	$\beta$ ( $^{\circ}$ )	$r$ (AU)	$\alpha$ ( $^{\circ}$ )	Telescope Code*
2017 October 3	19.2	8.4	1.12	11.3	3
2017 October 15	23.5	9.3	1.08	8.7	2
2017 October 15	23.5	9.3	1.08	8.7	3
2017 October 16	24.2	9.4	1.07	8.7	2
2017 October 17	24.2	9.4	1.07	8.7	2
2017 October 17	24.2	9.4	1.07	8.7	4
2017 October 25	27.1	9.9	1.07	10.1	2 - event
2017 October 27	27.9	10.1	1.07	10.7	2 - event
2017 October 28	28.2	10.1	1.07	11.00	1 - event
2017 October 28	28.2	10.1	1.07	11.00	2
2017 October 29	28.9	10.2	1.07	11.4	1
2017 October 30	28.9	10.2	1.07	11.7	1
2017 October 31	29.2	10.3	1.07	12.0	1
2017 November 1	29.7	10.4	1.07	12.5	1
2017 November 2	30.1	10.5	1.07	12.9	1
2017 November 15	35.3	11.2	1.12	18.2	5
2017 November 22	38.1	11.6	1.15	20.9	3 - event
2017 November 23	38.5	11.7	1.16	21.23	3 - event
2017 December 12	46.1	12.6	1.28	26.7	2 - event

\* see Table 2

---

**Table 2:** List of the observers with their facilities.

<b>Observers</b>	<b>Observatory</b>	<b>Aperture (m)</b>	<b>Code</b>
Berthier, J., Descamps, P., Normand, J., Vachier, F.	Haute-Provence Observatory IAU code #911	1.20	1
Wiggins P.	IAU code #718 112°18'E 40°38'N	0.35	2
De Groot, H.	IAU code #C39 5°47'57"E 51°49'46"N	0.35	3
Coudert, J., Labrevoir, O., Marcon, J.-P., S. Olimpiade and pupils of Lycée Victor Hugo, Carpentras, France	Haute-Provence Observatory IRIS Telescope Centre d'astronomie de Saint- Michel l'Observatoire	0.50 0.60	4
Chojnacki, V. with pupils of Lycée Esclangon, Manosque, France	Haute-Provence Observatory IRIS Telescope	0.50	5

---

**Table 3:** – Solutions of the inhomogeneous Roche problem. The bulk porosity includes the small-scale microporosity and the large-scale macroporosity (empty space). The primary and the secondary are described by their semi-axes  $(a_p, b_p, c_p)$  and  $(a_s, b_s, c_s)$ . The relative separation  $D$  is defined as  $(a_p + a_s)/d$ , where  $d$  is the orbital separation of the system. Values of macroscopic physical parameters (grain densities and bulk porosities) are intrinsically connected with the adopted model of internal density distribution.

Synodic period (h)	$\Omega$	q	n	$\rho_b$ (g/cm <sup>3</sup> )	$\rho_g$ (g/cm <sup>3</sup> )	p	$b_p/a_p$	$c_p/a_p$	$b_s/a_s$	$c_s/a_s$	D
50.826	0.033	0,88	9	4.02	28.1	86%	0.746	0.676	0.699	0.637	0.207

**Table 4:** –Resolution of the system [5] for two pairs of dates.  $l_{sep}$  is the latitude of the sub-Earth point. J2000 equatorial coordinates of (3905) Doppler are given for each epoch. The pole solutions are given in J2000 equatorial coordinates.

31 October 2013			27 October 2017			Pole 1		Pole 2	
$\alpha$ (°)	$\delta$ (°)	$l_{sep}$ (°)	$\alpha$ (°)	$\delta$ (°)	$l_{sep}$ (°)	$\alpha_0$ (°)	$\delta_0$ (°)	$\alpha_0$ (°)	$\delta_0$ (°)
36.98	40.1 7	0±0.3	13.28	26.50	5±0.5	89.4	-35.9	239.7±5	47.5±5
31 October 2013			22 November 2017			Pole 1		Pole 2	
36.98	40.17	0±0.3	8.19	25.61	3±0.5	77.5	-42.0	241.0±5	47.2±5

**Figure 1:** List of oppositions of Doppler in the interval 2013-2055 reported in ecliptic longitudes. In blue the Earth orbit and in red the Doppler orbit. Doppler was discovered as a double system during the 2013 perihelic opposition. *P* is the perihelia and *N* the ascending node.

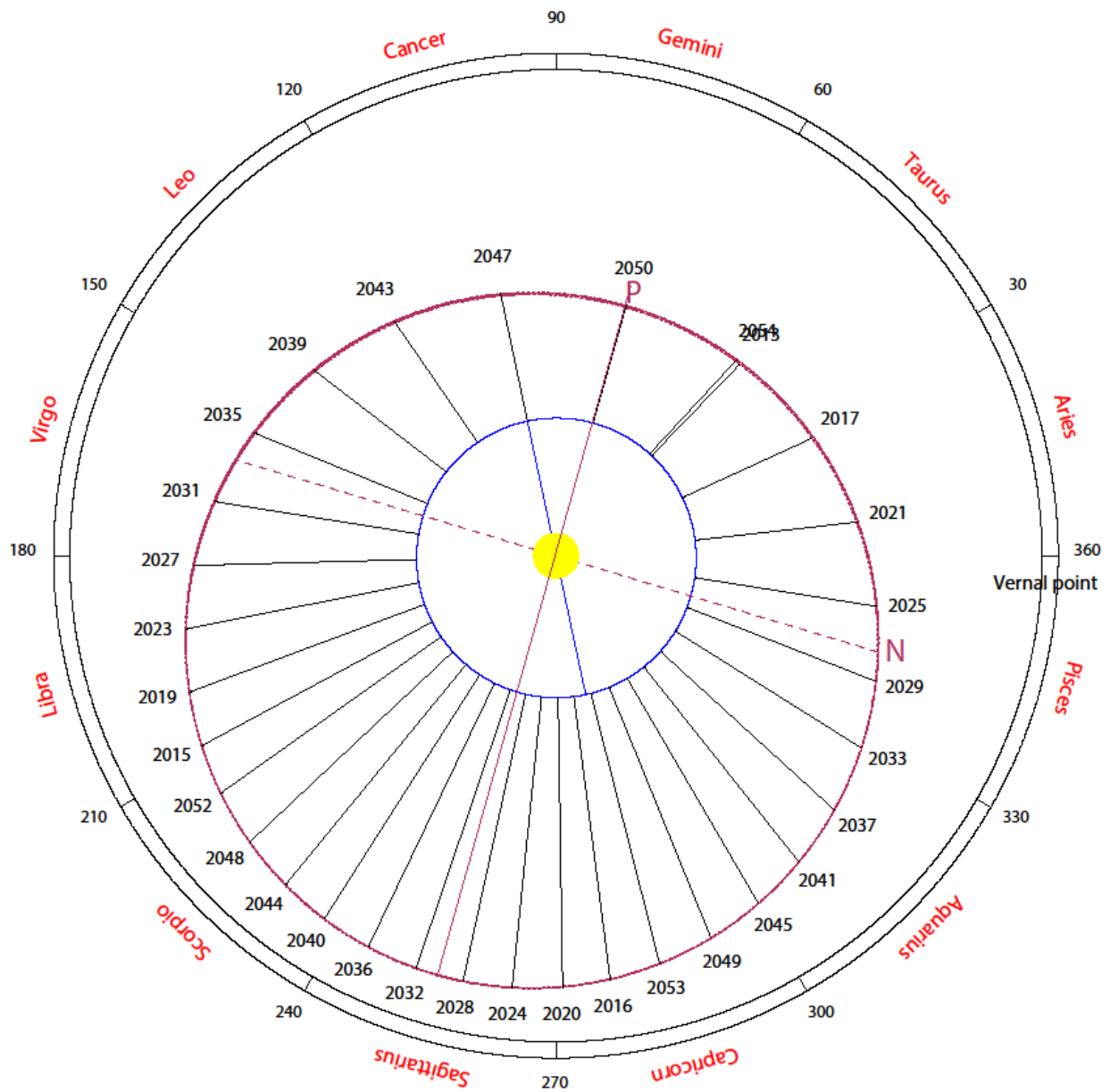


**Figure 2:** PDM plot of  $\theta$  vs. period. The minimization of  $\theta$  is obtained for  $P = 2,11778$  days (50.826h).

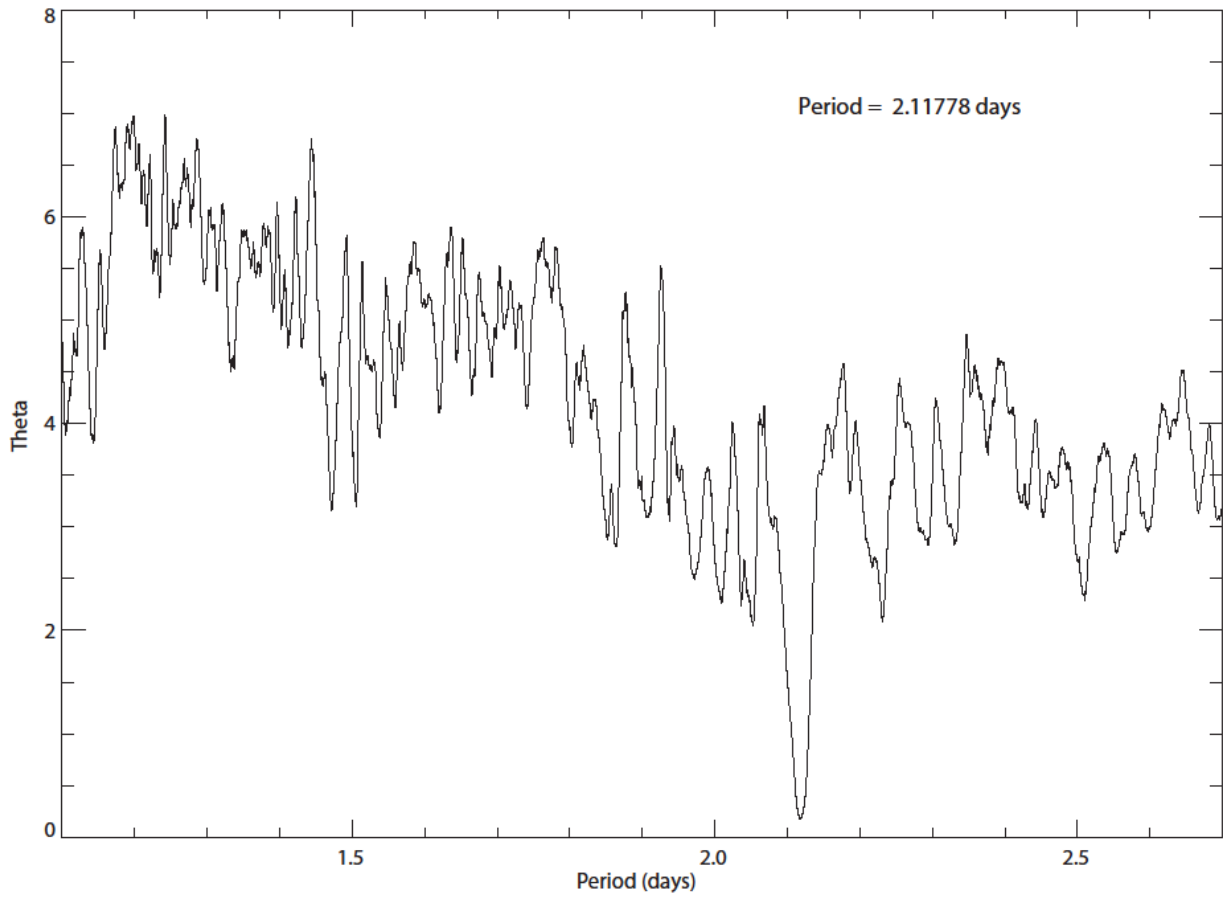


**Figure 3:** Composite light curve from 2017 photometric data

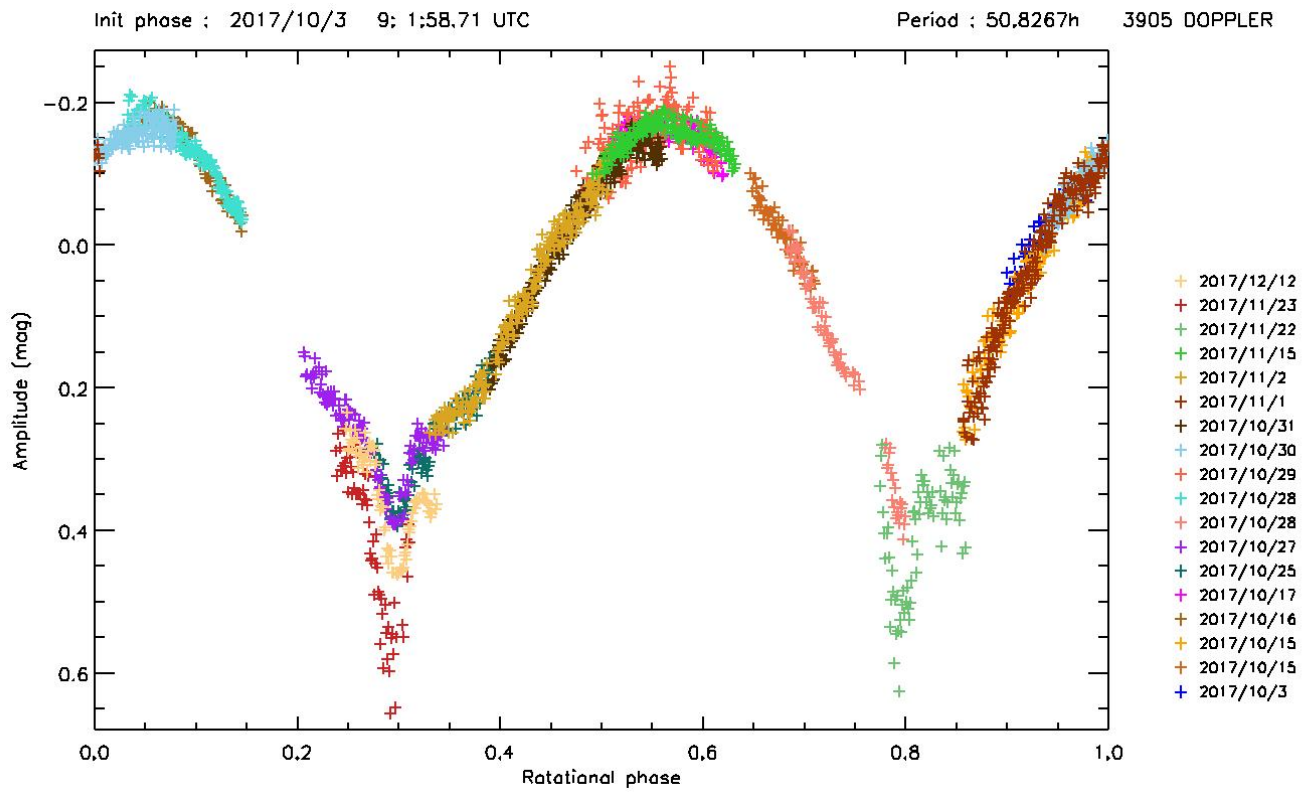
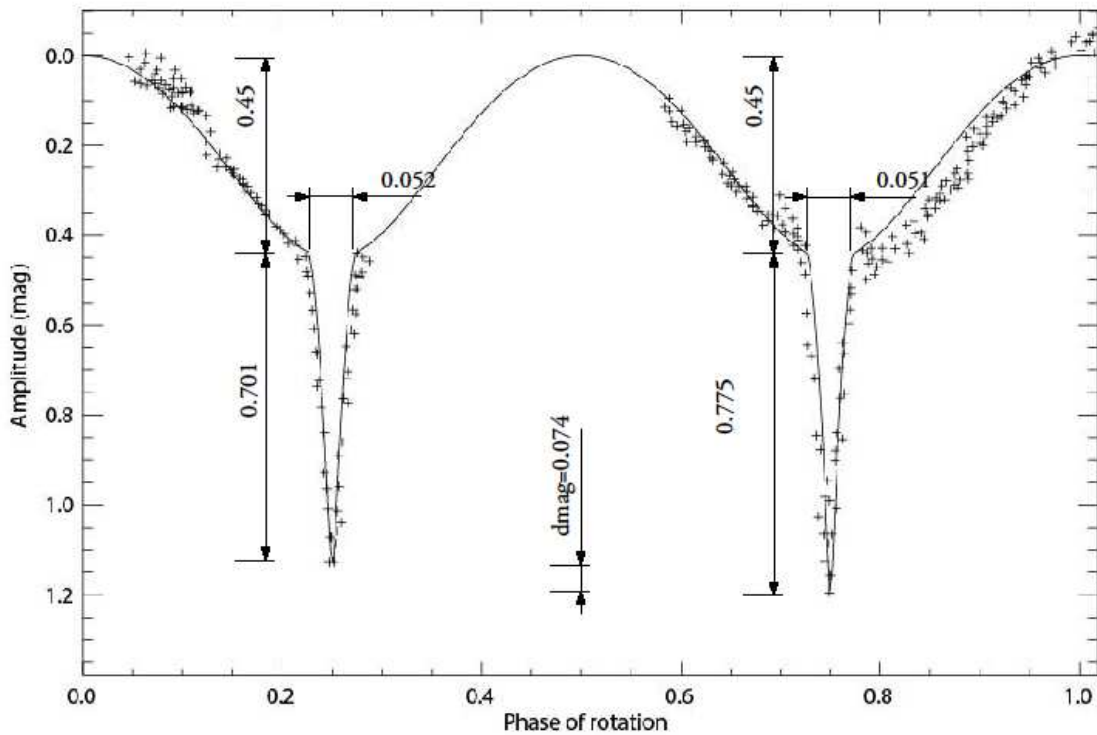


**Figure 4:** Synthetic light curve superimposed to the light curve of Doppler observed in 2013. Durations of the events are shown as well as the amplitudes of the rotational light curve (0.45 mag) and the magnitude drops (0.701 mag and 0.775 mag). The durations should be equal. The amplitude of the first drop depends only on the mass ratio of the components. The amplitude of the second drop depends on both the mass ratio and the limb darkening parameter. The duration of an event depends on the bulk density and, to a lesser extent, on the mass ratio. Therefore, from the graphical analysis of the light curve, we can unambiguously determine the type of light scattering by the surfaces, the mass ratio between components and the bulk density as well.



---

**Figure 5:** Synthetic light curves resulting from the solution obtained for the binary system of Doppler. The effect of the latitude of the sub-Earth point shows that very quickly, as soon as the orbital plane of the system is sufficiently inclined over the line of sight, the events disappear.

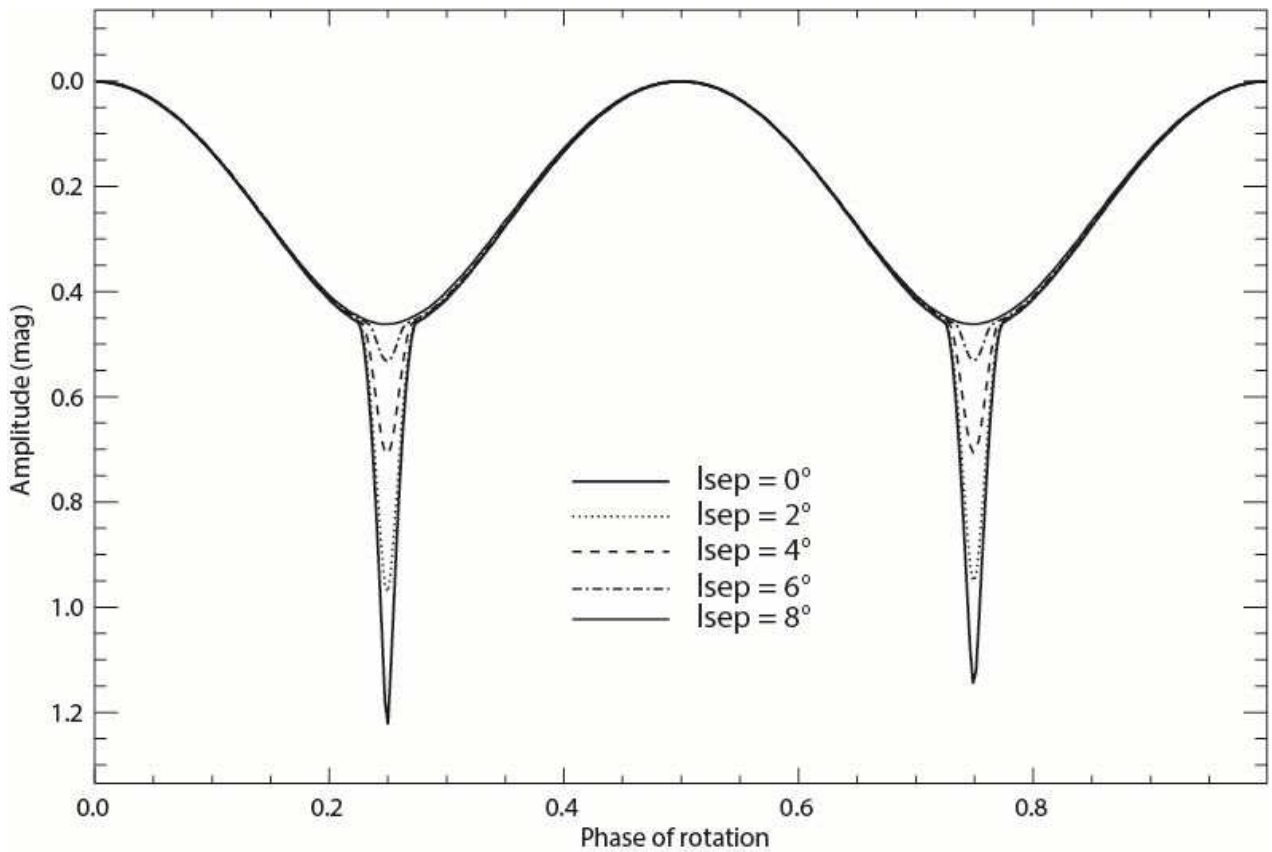


**Figure 6:** Evolution of the amplitude of the light curve of Doppler and the magnitude differential as a function of the latitude of the sub-Earth point. In October and November 2017, small amplitude events were detected, which makes it possible to estimate the value of the latitude of the sub-Earth point for these epochs required for deriving the pole orientation.

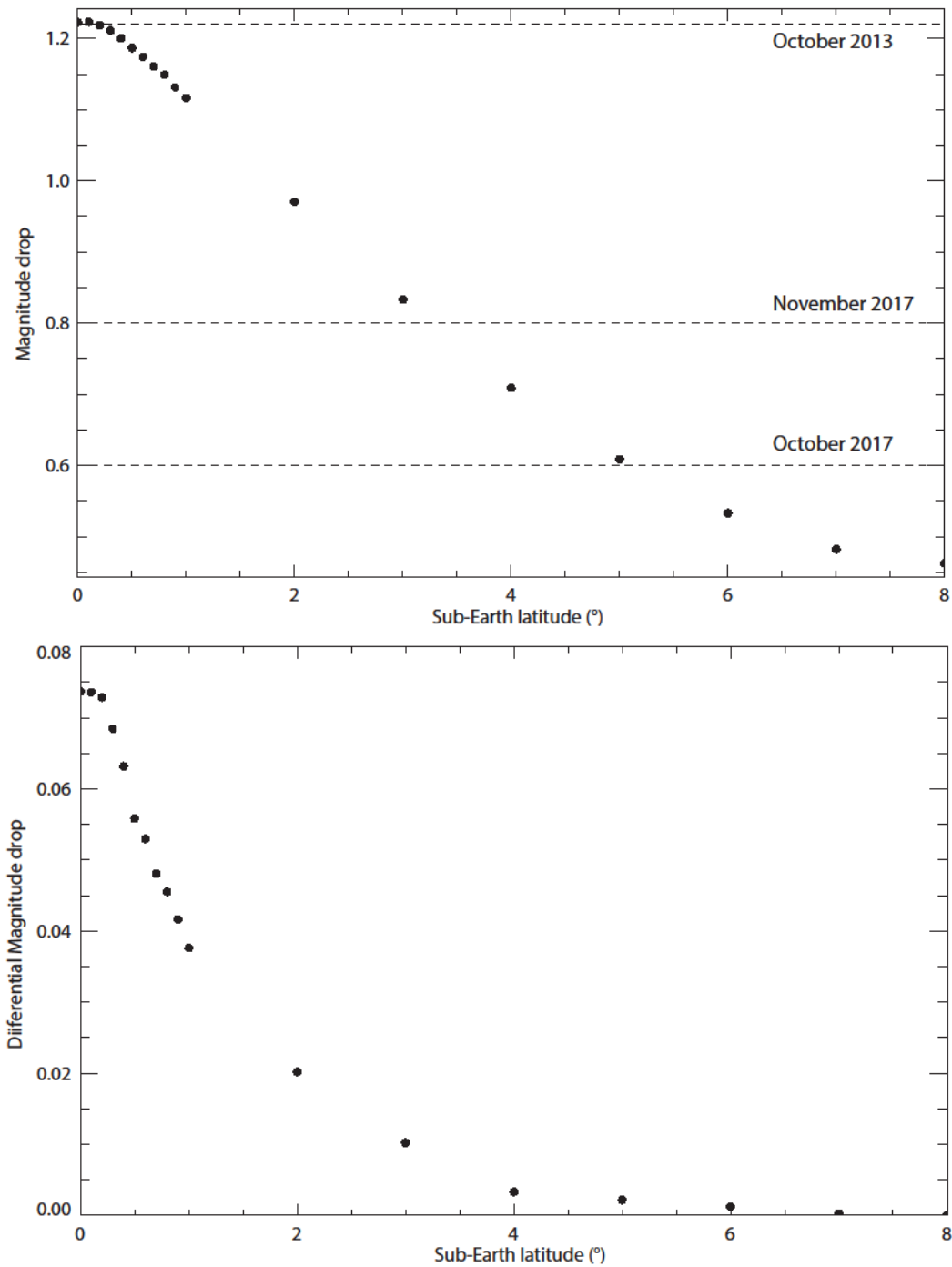
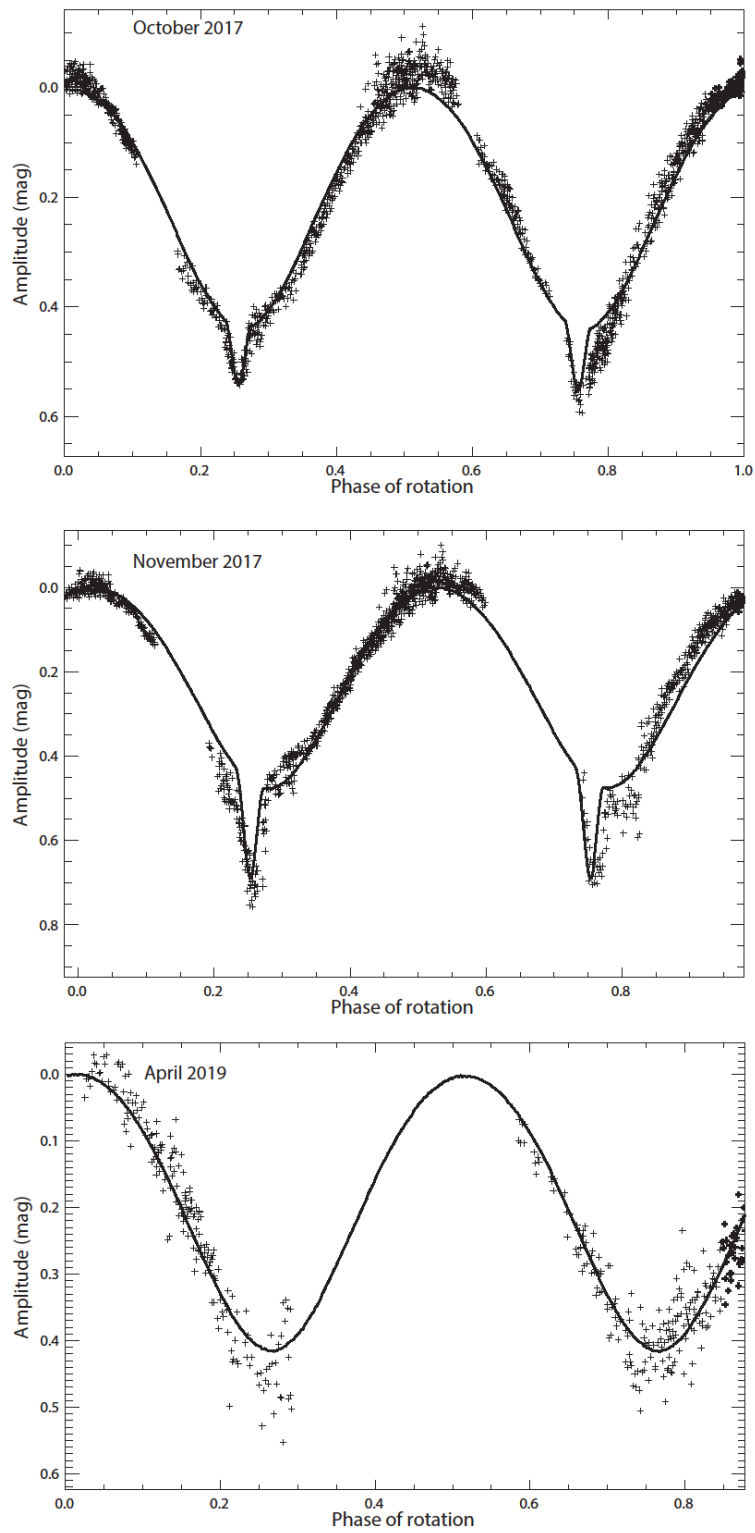


**Figure 7:** Fitted synthetic light curves superimposed to the photometric observations of 2017 and 2019.



---

**Figure 8:** Full events detected on the same minima on October, 27 and December, 12. Owing to the fact that the phase angle was important, the phase effects and mutual shadowing play a crucial role in defining the morphology of the light curve.

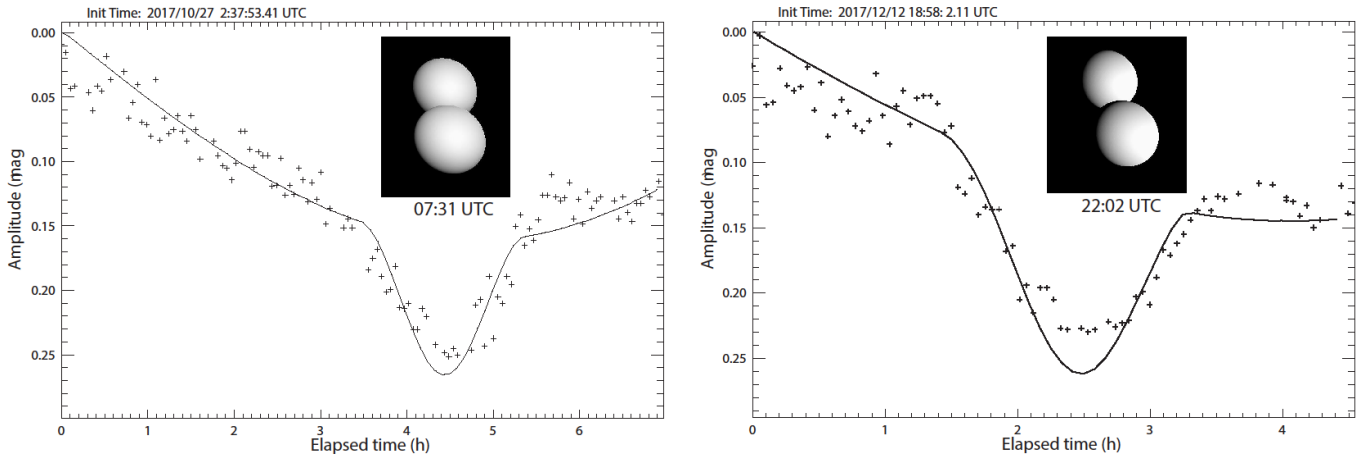


**Figure A.1:** Schematic diagram of a double system whose components are spherical.

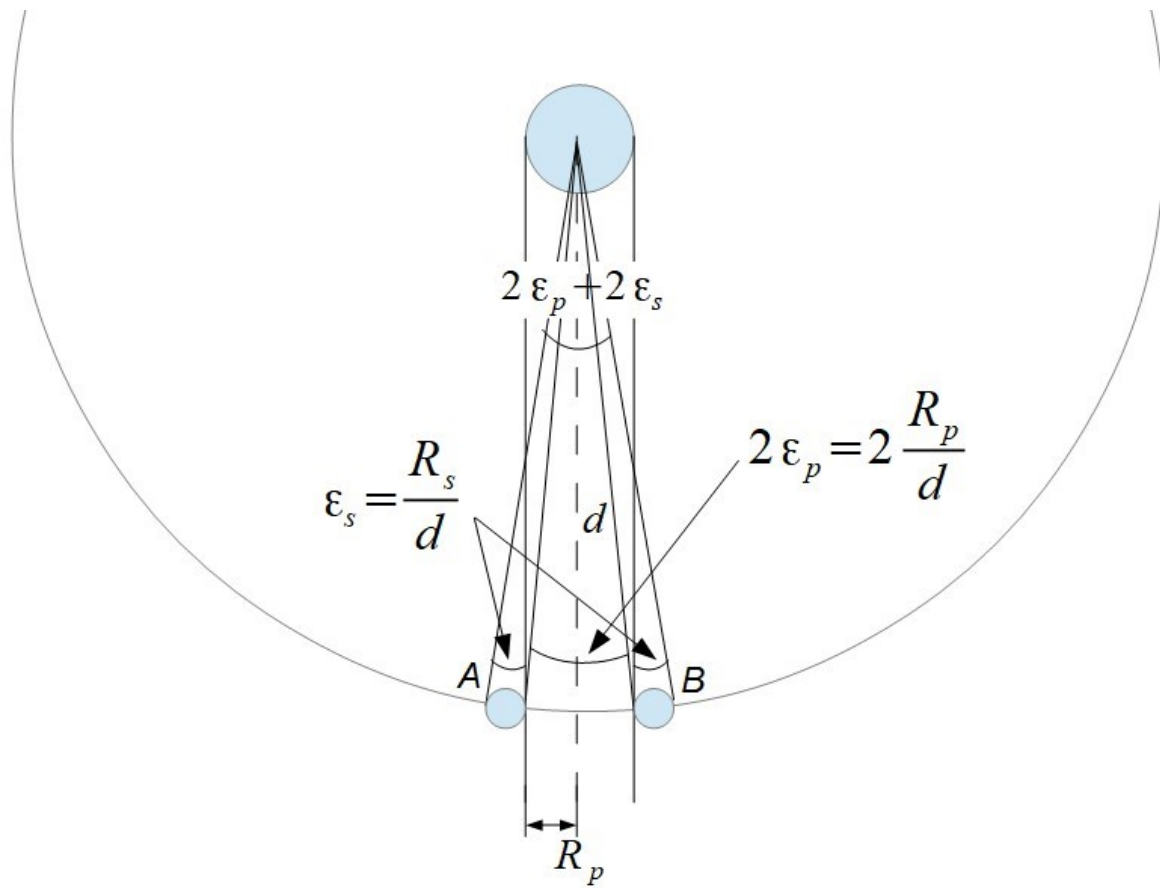


**Fig. B.1:** System of coordinates used to compute magnitude drops during an occultation event inside a binary asteroid in edge-on configuration. The photometric equator is the great circle passing through the subsolar and sub-earth points. Photometric longitude,  $\lambda$ , is measured along the photometric equator, and photometric latitude,  $\varphi$ , is measured along the central meridian which is the perpendicular great circle (see text for further explanations).

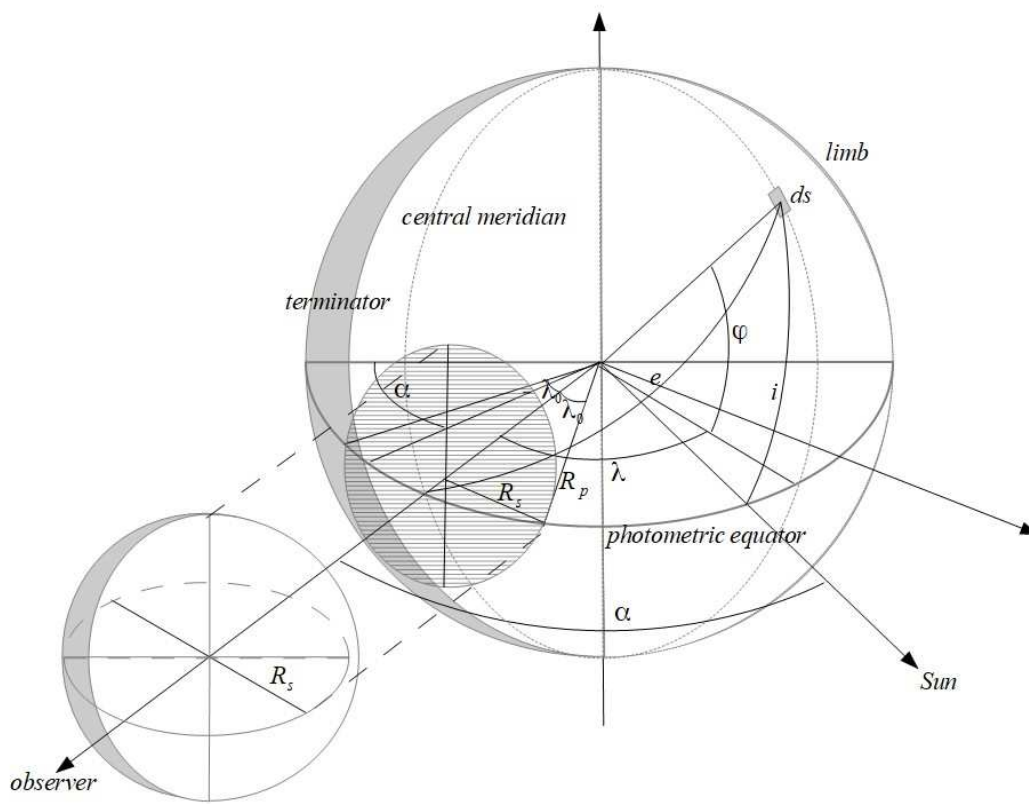


**Fig. B.2:** Offset in magnitude between minima as a function of phase angle,  $\alpha$ , mass ratio,  $q$ , and limb darkening parameter,  $k$ .

